TU Delft

Delft University of Technology

Document Version
Final published version

Licence
Dutch Copyright Act (Article 25fa)

Citation (APA)
Wakeham, N. A., Van Weers, H. J., Houmes, M. J. A., Baglioni, G., Davidovikj, D., Dercksen, J. P. C., Šiškins, M., Steeneken, P. G., Van der Zant, H. S. J., & More Authors (2026). Determination of vibration eigenfrequencies and eigenmodes of transition-edge sensor microcalorimeters for NewAthena X-IFU. *Journal of Astronomical Telescopes, Instruments, and Systems*, *12*(2), Article 026004. https://doi.org/10.1117/1.JATIS.12.2.026004

Important note
To cite this publication, please use the final published version (if applicable).
Please check the document version above.

Copyright
In case the licence states “Dutch Copyright Act (Article 25fa)”, this publication was made available Green Open Access via the TU Delft Institutional Repository pursuant to Dutch Copyright Act (Article 25fa, the Taverne amendment). This provision does not affect copyright ownership.
Unless copyright is transferred by contract or statute, it remains with the copyright holder.

Sharing and reuse
Other than for strictly personal use, it is not permitted to download, forward or distribute the text or part of it, without the consent of the author(s) and/or copyright holder(s), unless the work is under an open content license such as Creative Commons.

Takedown policy
Please contact us and provide details if you believe this document breaches copyrights.
We will remove access to the work immediately and investigate your claim.

This work is downloaded from Delft University of Technology.

JATIS Journal of Astronomical Telescopes, Instruments, and Systems

RESEARCH PAPER

Determination of vibration eigenfrequencies and eigenmodes of transition-edge sensor microcalorimeters for NewAthena X-IFU

Nicholas A. Wakeham,[a,b,*,†] Henk J. van Weers,[c,†] Maurits J. A. Houmes,[e] Gabriele Baglioni,[e] Dejan Davidovikj,[e,f] Johannes P. C. Dercksen,[c] Makars Šiškins,[e] Simon R. Bandler,[b] James A. Chervenak,[b] Fred M. Finkbeiner,[d,b] Brian D. Jackson,[c] Stephen J. Smith,[b] Peter G. Steeneken,[e] Edward J. Wassell,[b] and Herre S. J. van der Zant[e]

[a]University of Maryland Baltimore County, CSST, Baltimore, Maryland, United States
[b]NASA Goddard Space Flight Center, Greenbelt, Maryland, United States
[c]SRON Space Research Organisation Netherlands, Leiden, The Netherlands
[d]Sigma Space Corp./Hexagon US Federal, Lanham, Maryland, United States
[e]Delft University of Technology, Kavli Institute of Nanoscience Delft, Delft, The Netherlands
[f]Balthazar Labs B.V., Amsterdam, The Netherlands

ABSTRACT. The X-ray Integral Field Unit (X-IFU) is an instrument being developed for the New Advanced Telescope for High ENergy Astrophysics observatory satellite. It utilizes an array of X-ray transition-edge sensor (TES) microcalorimeter pixels, with the instrument designed to achieve an energy resolution of 4 eV at photon energies up to 7 keV. Vibration of individual TES pixels in the array has the potential to degrade this performance predominantly through time-varying thermal dissipation. To mitigate this, in the X-IFU design, the first vibrational eigenfrequency of the TES pixels is required to be greater than 25 kHz. This is to ensure that the first eigenfrequency is significantly larger than the bandwidth of known vibration drivers, such as cryocoolers, and therefore coupling and dissipation in the pixels is negligible. We present theoretical and experimental determination of the eigenfrequencies and eigenmodes of prototype TES pixels designed for X-IFU. We show that the first eigenfrequency is 89 kHz at room temperature and decreases to 86 kHz at 5.6 K.

© 2026 Society of Photo-Optical Instrumentation Engineers (SPIE) [DOI: 10.1117/1.JATIS.12.2.026004]

Keywords: microvibration; X-ray; microcalorimeter

Paper 250170 received Oct. 15, 2025; revised Apr. 15, 2026; accepted Apr. 17, 2026; published May 14, 2026.

1 Introduction

The New Advanced Telescope for High ENergy Astrophysics (NewAthena) is a European Space Agency (ESA) led X-ray observatory satellite due for launch in the 2030s. The mission is designed to investigate the "Hot and Energetic Universe" through measurements of the chemical and physical properties of energetic plasmas.[1] One of the instruments on NewAthena is the X-ray Integral Field Unit (X-IFU), which will have an array of 1504 transition-edge sensor (TES) microcalorimeter pixels designed to detect X-rays in the range of 0.2 to 12 keV with an energy resolution of 4 eV at energies up to 7 keV.[2,3]

*Address all correspondence to Nicholas A. Wakeham, nwakeham@umbc.edu

†These authors contributed equally to this work.

2329-4124/2026/$28.00 © 2026 SPIE

X-ray TES microcalorimeters designed for X-IFU consist of a Mo/Au superconducting bilayer strongly thermally connected to a Bi/Au bilayer X-ray absorber. The TES is weakly thermally connected to a thermal bath, with the bath temperature less than the superconducting critical temperature $T_c \sim 90$ mK. The superconductor is maintained in the resistive transition through Joule heating in the TES in a voltage bias circuit to provide electro-thermal feedback. When an X-ray photon is absorbed in the device, the incident energy causes a small temperature increase, increasing the TES resistance before it returns to its quiescent point. This change in resistance is measured as a current change in the TES by inductively coupling to a superconducting quantum interference device. The magnitude of the resulting current pulse is a highly sensitive monotonic function of the energy of the incident photon.[4]

Achieving the state-of-the-art energy resolution required for the X-IFU necessitates careful control and understanding of every aspect of the instrument system.[2] One area of interest is the effect of vibration on each component of the instrument during operation. These vibrations may be driven by the movement of mechanical parts or gas in the cooling chain and then transferred through the components of the instrument to the individual pixels of the detector. At each stage, the vibrations may result in thermal dissipation. In the case of a constant dissipation, this leads to a constant heat load that must be accounted for. However, more significantly, a time-varying dissipation may lead to temperature instability and variation in the gain scale of components in the readout chain. In particular, time-varying thermal dissipation at each TES microcalorimeter pixel could cause variation in the detector gain scale that cannot be corrected and therefore a degradation in the energy resolution.[5,6] In the engineering model of the ASTRO-H mission, microvibrations from coolers caused significant and unacceptable temperature instability at the microcalorimeter spectrometer that had to be corrected in the flight models of ASTRO-H and XRISM.[5,7] Analysis of the thermal performance of ESA's Plank mission in orbit showed there was significant heating of the bolometer stage from microvibrations.[8] ESA has therefore established a microvibration working group for X-IFU to study the impact of microvibrations on the cryogenic chain and instrument performance during the development phases.

To understand the potential impact of vibration-induced thermal dissipation, we must understand the eigenfrequencies and eigenmodes of each part of the instrument. In the case of the large-scale mechanical components, including the detector mounting stage and the silicon detector chip, this can be done using finite element modeling supported by readily available vibrometer and thermometer measurements.[9–11] However, each microcalorimeter pixel occupies $\sim 300 \times 300 \times 7$ μm and has a mass of only ~ 4 μg. Therefore, measuring the vibration response of these very small pixels presents additional challenges. Furthermore, we are interested in the vibration properties of the pixels while the X-IFU is operational, and therefore, they must be determined at temperatures sufficiently close to the operating temperature of 55 mK.

In this report, we present a study of the eigenfrequency and eigenmodes of a TES microcalorimeter pixel design that was the prototype for X-IFU in 2022. We explore two different experimental techniques to measure the vibrational response of the pixels at room temperature using conventional single-spot laser interferometry and using Digital Holographic Microscopy (DHM®). These measurements are compared with finite element modeling of the expected eigenfrequencies and eigenmodes of our pixel design. The model is then used to explore how different design parameters influence the first eigenfrequency. We also present preliminary measurements of the response of the pixels at 6 K and compare this to the expected temperature dependence.

Preliminary analysis by the X-IFU microvibration working group has established a requirement that the first eigenfrequency of the microcalorimeter pixels be >25 kHz to ensure that it is significantly larger than the bandwidth of known vibration drivers, such as cryocoolers, and therefore, coupling and dissipation in the pixels are negligible. We show here that at room temperature and 6 K, the first eigenfrequency is significantly larger than the 25-kHz requirement.

2 Methods

2.1 TES Microcalorimeter Pixel Design

The general design of TES microcalorimeter pixels for the X-IFU is shown schematically in three-dimensions (3D) in Fig. 1(a). Figure 1(b) shows the dimensions of the specific design tested in this work in a two-dimensional (2D) drawing viewed from above. This pixel design was the

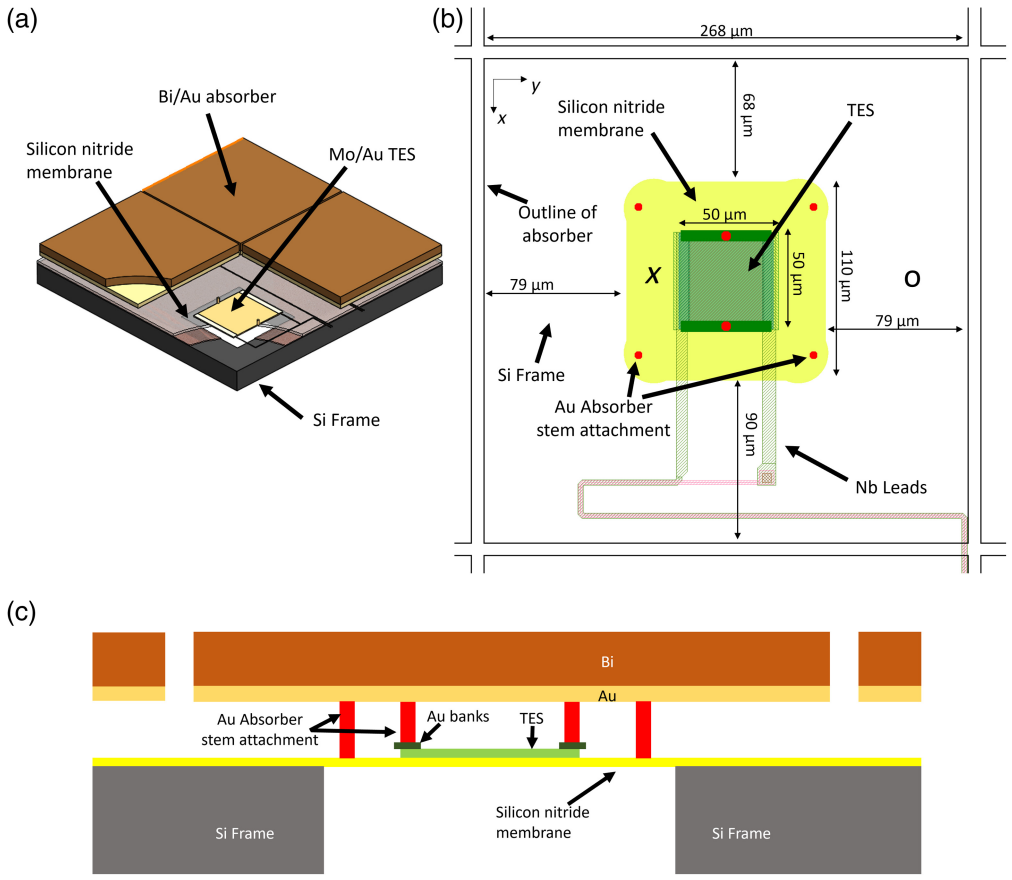
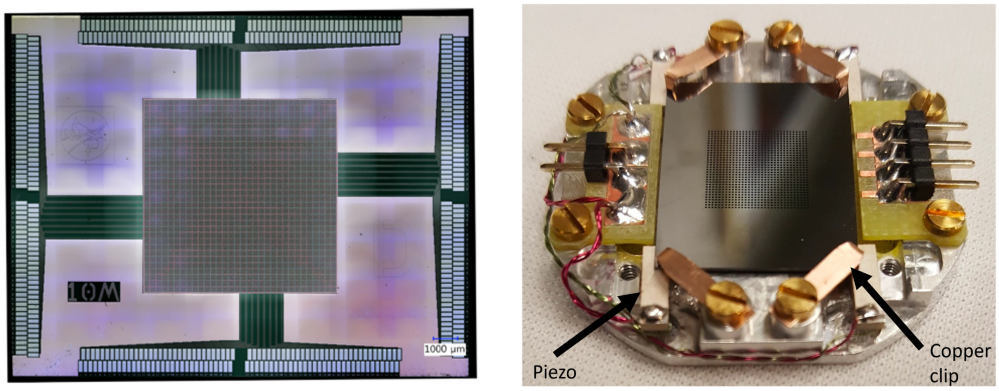


Fig. 1 Transition-edge sensor microcalorimeter pixel design. (a) 3D schematic diagram of a typical Mo/Au TES microcalorimeter for X-ray detection. This shows the Si wafer is etched from the back to leave the Mo/Au TES only supported by a silicon nitride membrane. The Si chip then forms a frame structure around each pixel. The Bi/Au absorber is supported above the TES by pillar stems on the TES. (b) Top view of the TES pixel design studied in this work. The absorber is only shown as an outline for clarity. Note that the center of the absorber is offset from the center of the TES. The X and O indicate the approximate position of the laser spot during the interferometry measurement of the pixel and Si frame, respectively, described in detail in Sec. 2.2. (c) Schematic cross-sectional diagram of the TES pixel design.

prototype pixel design for X-IFU when the work was undertaken in 2022.[12] The TES was a 50×50 µm Mo/Au bilayer. The thickness of the Mo layer was 41.5 nm, and the thickness of the Au layer was 223 nm. Electrical connections were made to this superconducting bilayer with Nb leads at each end. Au banks were placed along the edges of the bilayer. These had a width of 6 µm and a thickness of 180 nm. The TES was fabricated on top of a 0.5-µm-thick silicon nitride layer that was continuous across the entire 300-µm-thick silicon wafer. Behind each TES, a square region of the silicon chip of side length 110 µm was etched away. We call this the silicon nitride membrane region. Removing the Si in this region caused the TES to be only thermally and mechanically connected to the silicon chip by the silicon nitride membrane.

An Au/Bi bilayer absorber ensures the required X-ray absorption in the energy band needed for X-IFU. In the tested devices, the thicknesses of the layers were 1.5 µm of Au and 3.1 µm of Bi. The absorber was a square with a side length of 268 µm. This X-ray absorber was thermally connected to the TES through two Au pillar stems between the banks on the TES and the absorber. These stems had a diameter of 5 µm and a height of 4.3 µm. The absorber was therefore mechanically supported 4.3 µm above the plane of the TES by these stems, as well as four other stems between the corners of the silicon nitride membrane region and the absorber. These pillar stems in the corners had the same length as the others but a diameter of 4 µm. Figure 1(c) shows a schematic cross-sectional diagram of the pixel design.



(a) (b)

Fig. 2 (a) View from above of the transition-edge sensor microcalorimeter chip used for vibration measurements. The chip is 15 mm × 19 mm with an array of 1024 pixels in the center. (b) Kilopixel chip mounted for laser interferometry measurements with the four corners held with copper clips to piezo actuators. The chip was mounted upside down so that the laser light could be passed through the silicon nitride membrane and reflected off the relatively smooth surface of the Au layer of the X-ray absorber.

Note that in the tested design, the absorber was not centered along the x-axis relative to the TES, as shown in Fig. 1(b). This meant that in the x direction, one absorber edge was 68 µm from the edge of the silicon nitride membrane region, and the other absorber edge was 90 µm from the edge of the membrane region. This asymmetry has the advantage of giving more space for routing the Nb leads but is largely an arbitrary choice and is not a necessary condition for the design.

The tests presented below were performed on a 15 × 19 mm prototype Si chip with an array of 1024 TES microcalorimeter pixels in the center, as shown in Fig. 2(a). Note that the pixel designs studied were the flight design for X-IFU in 2022, as stated above, but the Si chip design was significantly different from the ∼85-mm-diameter hexagonal chip that will be used in flight.

2.2 Measurement Techniques

Two techniques were used to measure the vibration eigenfrequencies of the individual TES pixels. The first was laser interferometry using a single HeNe (633 nm) laser spot with a spot diameter of ∼10 µm. In this technique, the chip was placed on top of four piezo actuators at the corners and held in place at these points by flexible copper clips, as shown in the photograph of the setup in Fig. 2(b). The chip was placed upside down, so that the laser light passed through the transparent silicon nitride membrane region and was reflected off the layer of 1.5 µm of Au of the absorber. The laser was aimed ∼40 µm from the pixel center at approximately position X shown in Fig. 1(b). This position was chosen to allow the light to avoid the Si frame and the TES and reflect off of the absorber. This smooth gold layer provided better signal-to-noise than the rough Bi surface on the front of the chip.

The detector chip was excited by applying a sine wave AC voltage to the piezo actuators of amplitude V_{pz} and known frequency. The four piezos were connected in parallel to ensure the signal at each was approximately equal in magnitude and phase. The reflected light intensity also varied sinusoidally and was measured by a photodiode with the resultant voltage signal fed into a vector network analyzer (VNA). $|S_{21}| = 20\log_{10}(V_{pd}/V_{pz})$ was recorded from the VNA, where V_{pd} is the oscillation amplitude of the photodiode response. V_{pd}/V_{pz} is approximately proportional to z_m/z_{pz}, where z_m is the displacement magnitude in the z direction at the measurement point, in this case, the pixel. z_{pz} is the displacement magnitude of the piezo actuators. Therefore $|S_{21}|$ is a measure of the displacement ratio of the pixel to the piezo actuators. A resonant vibration response at the pixel can be identified as a peak in $|S_{21}|$ above the background response.

Measurements were also performed with the laser beam reflected off the Si frame among the pixels. This was then a measure of the vibration response of the whole Si chip. By identifying resonant peaks in $|S_{21}|$ that were present in the pixel response but not the chip, we were able to

distinguish between vibration eigenfrequencies of the silicon chip and the pixel. The measurements were all performed with the setup under vacuum, and the chamber could be cooled to ~6 K to measure the eigenfrequencies at low temperature.[13] It is important to note that the measurement system is uncalibrated, and therefore, the absolute value of $|S_{21}|$ cannot be used to interpret the absolute magnitude of the displacement vibrations measured at different locations and at different temperatures. It can only be used to determine the frequency of resonant responses.

The second technique to measure the vibration response of the pixels was using the commercially available Digital Holographic Microscope (DHM®) from Lyncée Tec.[14,15] In this technique, a charge-coupled device (CCD) camera was used to record a hologram produced by the interference between a reference light wave and one reflected from the absorber array. Digital processing was then performed to reconstruct a 3D image from this hologram. The benefit of this technique is the ability to simultaneously obtain the relative height of all points in the microscope field of view in a single image without scanning. This can then be combined with a vibration actuator and stroboscopic measurement to record a video of the vibration response of the entire absorber of a pixel as a function of actuation frequency. In this way, we were able to clearly image the vibration modes of the absorbers and measure their eigenfrequencies. The other advantage of this technique is that it is less sensitive to the surface roughness, so we were able to measure from reflection off the top of the absorber rather than having to measure through the silicon nitride membrane.

2.3 Finite Element Modeling

Finite element modeling was performed using COMSOL Multiphysics® to predict the eigenfrequencies and eigenmodes of the TES microcalorimeter pixels. The model is shown in Fig. 3. The absorber was modeled as two solid layers of the correct dimensions for the Bi and Au layers. The stems were also modeled as solid pillars and were connected to the absorber and silicon nitride membrane. The silicon nitride was only modeled for the region without Si behind it. This was modeled as a 2D shell with the appropriate thickness. The edge of the silicon nitride membrane was held as a fixed position constraint. The TES bilayer and Nb leads were not included in the model. The thickness of these layers is so small that they do not influence the predicted vibrational response significantly.

A pre-stress parameter was used in the model for the silicon nitride membrane because the fabricated layer is known to be under tensile stress. The exact value of the stress in this layer depends on the details of the fabrication and the temperature. A tensile stress of 0 to 100 MPa can be expected in the films used in the fabrication of the devices tested here based on prior measurements and manufacturer's specifications. However, we show below that our particular design is largely insensitive to this stress value.

The physical properties used for each of the materials in the model are shown in Table 1.

The mesh size in the model was chosen to be sufficiently small that further reduction in size did not significantly change the predicted eigenfrequencies or modes. The total modal mass

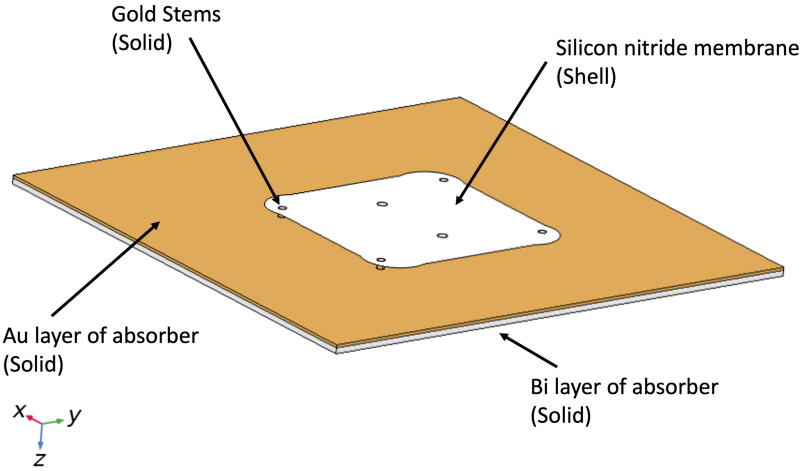


Fig. 3 COMSOL Multiphysics® finite element model used to model the vibration modes of the prototype microcalorimeter pixel design.

Table 1 Physical properties used for different materials in the finite element model.

	Young's modulus (GPa)	Poisson ratio	Density (kg m^{-3})
Silicon nitride	265 (Ref. 16)	0.23 (Ref. 16)	3180 (Ref. 17)
Gold	70 (Ref. 18)	0.44 (Ref. 18)	19,300 (Ref. 19)
Bismuth	32 (Ref. 20)	0.33 (Ref. 20)	9780 (Ref. 21)

fraction of the first eight modes in the z direction was found to be 91%, and including the first 12 modes in the z direction gave a total modal mass fraction of 99.5%.

3 Results

3.1 Eigenfrequency Measurements

Figure 4(a) shows the z-axis displacement magnitude relative to the input excitation measured with laser interferometry as a function of the excitation frequency of the piezo actuators at the four corners of the Si chip. The red dashed line shows the response measured when the laser light was reflected off the frame of the Si chip among individual pixels, indicating the excited resonances of the whole TES chip. The solid black line shows the response from the laser light reflected off the Au layer of the absorber of one pixel, as described above, and therefore shows the response of the individual pixel. In the pixel response, we observed two pixel vibration eigenmodes in the range of 80 to 100 kHz, one at 89 kHz and one at 97 kHz. There are no corresponding resonances in the chip response at these frequencies, indicating that these observed peaks are the excitation of pixel eigenmodes and not chip modes. Measurements below 80 kHz only showed coincident resonant peaks in both the pixel and chip response. Therefore, the peak observed at 89 kHz was assumed to be the first eigenmode.

To confirm the measured modes, DHM measurements were performed on this chip. In this measurement, the z displacement was measured simultaneously across many points on the Bi surface of the absorber. These results are shown in gray-scale in Figs. 4(b) and 4(c) at 89 kHz and 97 kHz, respectively. These results show qualitatively that, at these frequencies, the individual pixel vibration modes are being excited and show the mode shape at each frequency. Pixel vibration modes were also not observed below 89 kHz in this measurement. No additional unique pixel modes were observed with the DHM between 95 and 100 kHz, so the small additional peaks just above and below 97 kHz in the pixel interferometry measurements in Fig. 4(a) appear to be artifacts either of chip modes or interactions from neighboring pixels. This will require further investigation in the future.

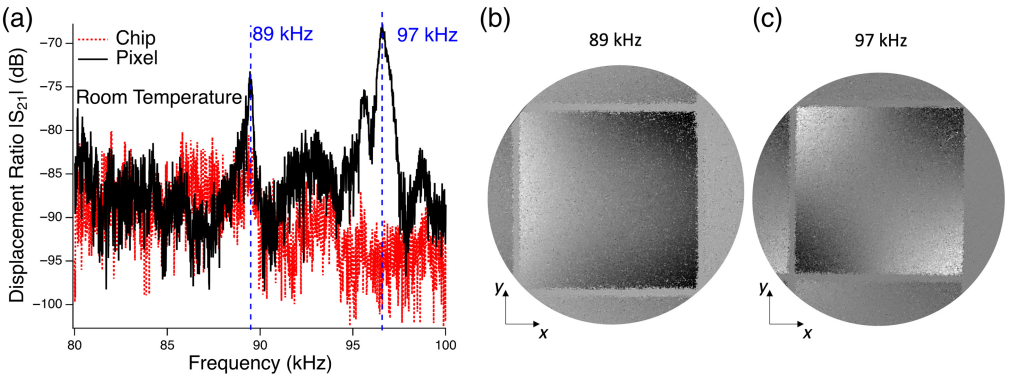


Fig. 4 (a) $|S_{21}|$ as a function of excitation frequency measured by laser interferometry from reflection from the Si frame (red dashed) and the pixel absorber (black solid). As described in Sec. 2.2, $|S_{21}| \propto z_m/z_{pz}$ where z_m is the displacement magnitude in the z direction at the measurement point and z_{pz} is the displacement magnitude of the piezo actuators. Digital holographic microscopy measurement with stroboscopic illumination of the (b) first pixel resonance at 89 kHz and the (c) second pixel resonance at 97 kHz. Contrast qualitatively shows z-axis displacement, where black indicates positive displacement and white indicates negative displacement.

The results shown in Fig. 4 are from a single TES pixel in the array. Other pixels in the array were also measured and showed consistent behavior, with only small variation in resonant frequencies of a few kHz. These differences likely arise from small variations in the fabrication of the pixels. Further detailed study of these subtle changes may be a future route to understanding non-uniformity in the fabrication and provide a means of identifying defects in arrays.

3.2 Finite Element Modeling

We can now compare these measured eigenmodes and eigenfrequencies with those calculated from the COMSOL model discussed above. Figure 5 shows the first three eigenmodes calculated for the prototype pixel design. The measured mode at 89 kHz agrees qualitatively with the predicted first mode shape shown in Fig. 5(a), with the diagonally opposite corners of the absorber moving out of phase with each other and the corners at the same x coordinate moving in phase. The second measured mode at 97 kHz corresponds to the third predicted mode shown in Fig. 5(c). This mode shows large displacement of the corners of the absorber, with diagonally opposite corners moving in phase. Note that Fig. 5 only shows the displacement of the absorber but the modes are also predicted to involve some movement in the membrane. The second predicted mode shown in Fig. 5(b) was not observed in the measurement. This predicted mode has an effective modal mass from translation in the z direction that is two orders of magnitude smaller than the first and third mode. Therefore, it is likely that this second mode was not significantly excited by the piezo actuators, which act predominantly in the z direction. The use of an excitation predominantly in the z-axis is not predicted to have affected our ability to determine the important first mode. The predicted modes also show that the offset between the center of the absorber and the center of the TES causes the degeneracy of equivalent modes in the x- and y-axes to be significantly broken and well separated in frequency, producing distinct modes at the first three eigenfrequencies.

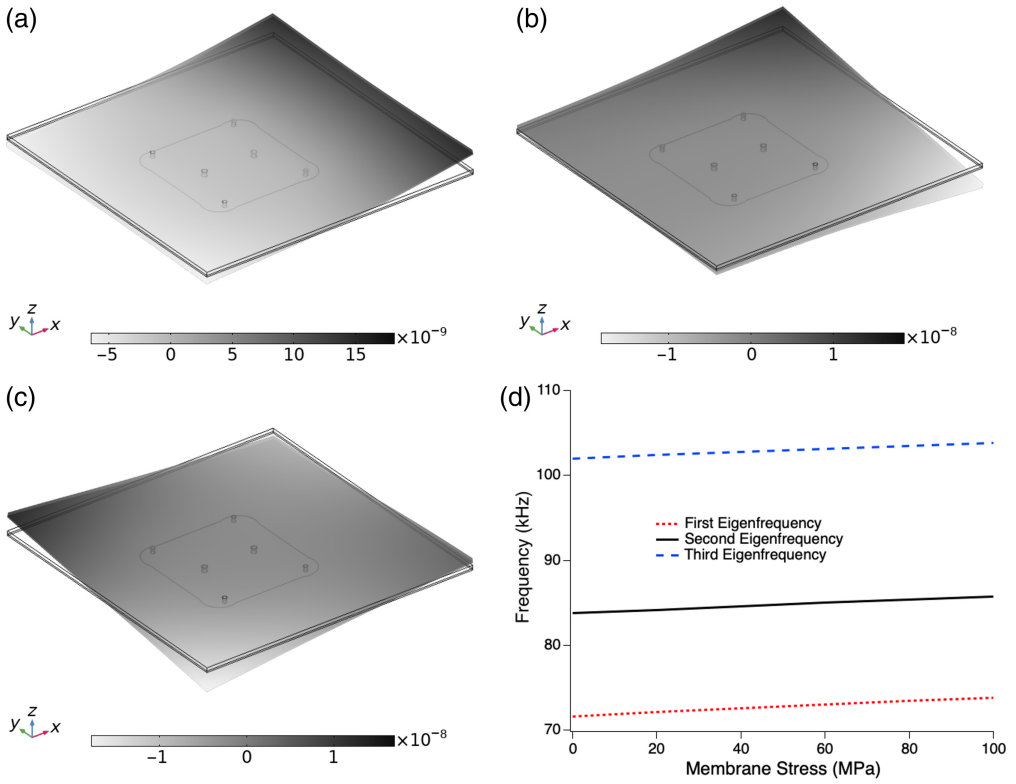


Fig. 5 (a)–(c) Predicted first three vibration eigenmodes of the prototype pixel design. Calculated using COMSOL Multiphysics®. Gray-scale shows z-axis displacement in arbitrary units. (d) Eigenfrequencies of each of these three modes as a function of the assumed initial in-plane stress of the silicon nitride membrane.

The eigenfrequencies of the first three predicted eigenmodes are shown in Fig. 5(d) as a function of the assumed initial in-plane stress of the silicon nitride membrane. This shows that in this design, the eigenfrequencies are not very sensitive to the assumed stress. However, the predicted first eigenfrequency is ~74 kHz in the expected range of stress; 74 kHz is ~15 kHz lower than the first measured resonant frequency of the pixels. The third predicted eigenfrequency has an average value of 104 kHz. This is ~7 kHz higher than the second measured resonant frequency. Note that the relative separation of the eigenfrequencies does not change with membrane stress, and therefore, no single value of stress will be able to reconcile the smaller-than-predicted separation between the first and third eigenfrequencies we measured.

It is interesting to consider the dependence of the first eigenfrequency on the pixel dimensions, to explore the apparent discrepancy between the measured and predicted eigenfrequencies, and for future optimization of the pixel design. Figure 6 shows the first eigenfrequency predicted from the COMSOL model as a function of different pixel design parameters while all other parameters are fixed at the values discussed in Sec. 2.1. In Fig. 6(a), the thickness of the Au or Bi layer of the absorber was varied, whereas all other parameters were kept fixed. The non-monotonic behavior with increasing thickness of the absorber is the result of the competing effects of the increasing stiffness of the absorber and the increasing mass. The first eigenfrequency

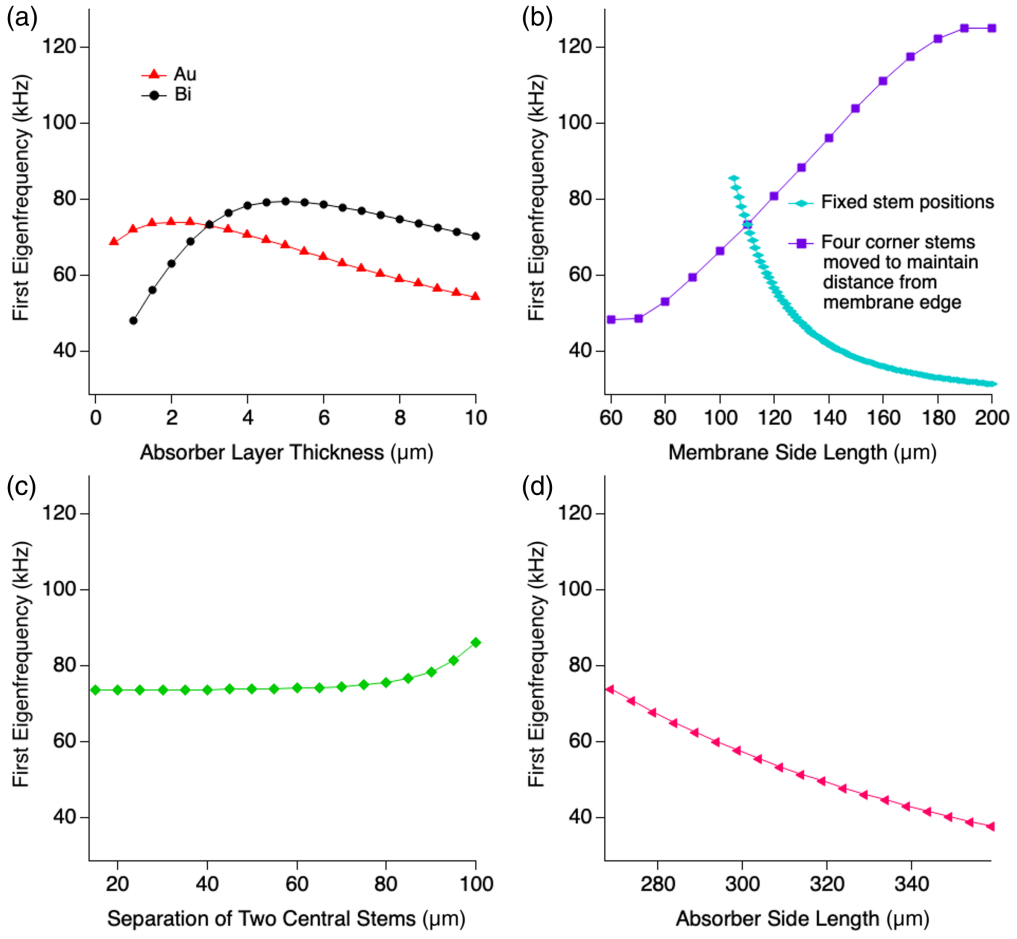


Fig. 6 First eigenfrequency predicted from finite element modeling as a function of different pixel design parameters. (a) First eigenfrequency as a function of the thickness of the Au (red triangle) and Bi (black circle) layer of the absorber. (b) First eigenfrequency as a function of the side length of the approximately square silicon nitride membrane. Blue squares show data assuming the absorber support stems are moved to maintain the same position relative to the edge of the membrane. Turquoise diamonds show data assuming the stem position is fixed as the membrane size changes. (c) First eigenfrequency as a function of the separation of two central support stems and therefore the TES width. (d) First eigenfrequency as a function of the side length of the square absorber, assuming membrane size and stem positions do not change.

initially rises as the absorber becomes more rigid, but eventually, it becomes effectively a rigid body, and then, the increasing mass is the dominant effect, causing the eigenfrequency to decrease. Figure 6(b) shows the first eigenfrequency as a function of the size of the approximately square silicon nitride membrane region. In the design shown in Fig. 1(b), this length was 110 μm. First, we assumed that as the membrane region changes size, the positions of four support stems at the corners of the membrane region are moved to maintain a fixed distance from these stems to the edge of the membrane region. This means that as the membrane gets larger, these four stems stay in the corners of the membrane and are further separated from the center and each other. The first eigenfrequency is quite sensitive to this parameter, particularly in the middle of the range shown. In this middle range, the membrane is significantly larger than the TES width, but significantly smaller than the absorber size. If instead we assume the stem position is fixed, then the model shows the first eigenfrequency falls rapidly as the membrane becomes larger and the membrane edge moves further away from the stems. Figure 6(c) shows the first eigenfrequency as a function of the separation of the two central support stems on the absorber. This shows that this has very little impact on the eigenfrequency until the separation becomes close to the membrane size. The TES bilayer is not included in the model, but in reality, the separation of these two central stems is set by the width of the TES. Therefore, this shows that the first eigenfrequency is largely insensitive to TES width. Finally, Fig. 6(d) shows the first eigenfrequency as a function of the side length of the square absorber. As expected, this shows that, if all other parameters are held fixed, the eigenfrequency falls rapidly as the absorber gets larger and the distance from the edge of the absorber to the support stems becomes larger. The dependence of the third eigenfrequency on these parameters is not shown in Fig. 6, but we find qualitatively similar correlations. In particular, close to the designed parameters, there are no small adjustments that can be made to simultaneously reconcile the discrepancy between the modeled and observed values of both the third and first eigenfrequencies.

3.3 Temperature Dependence

When in operation in the X-IFU, the silicon chip with the TES microcalorimeter array will be at 55 mK. Therefore, it is the eigenfrequencies at cryogenic temperatures that are relevant when considering the coupling of vibrational energy to individual pixels. To assess the behavior at low temperature, laser interferometry measurements of displacement were performed on the pixel design shown in Fig. 1(b) at 5.6 K at excitation frequencies up to 100 kHz. This was the lowest achievable temperature in the measurement apparatus. There are not expected to be significant changes in the mechanical properties of the pixels between 5.6 K and 55 mK, and therefore, this temperature is expected to be sufficient to describe the vibration response of the pixels during operation on the X-IFU.

The results from these low temperature measurements between 80 and 100 kHz, plotted in Fig. 7, show a single peak at 86 kHz. The second pixel resonance peak observed at room temperature is not apparent over the measured frequency range at 5.6 K. We are not able to distinguish from the available data whether the second resonant peak has been suppressed, has increased to frequencies greater than 100 kHz, or is obscured by an overlapping eigenfrequency of the Si chip.

Accurate modeling of the temperature dependence of the eigenfrequencies is extremely challenging because it requires knowledge of the low-temperature Young's modulus, coefficient of thermal expansion, and the residual stress of all the components. However, one effect we might anticipate is the change in the membrane stress as a result of the difference in the coefficient of thermal expansion between the silicon nitride membrane and the silicon chip. Although dependent on the specific properties of the silicon nitride deposition, typically the coefficient of thermal expansion is larger in silicon than in silicon nitride,[22–24] and therefore, we would expect a decrease in the membrane stress at low temperature. As shown in Fig. 4(d), the eigenfrequencies are expected to show a decrease due to a decrease in membrane stress, and therefore, this is qualitatively consistent with the small decrease in the first measured eigenfrequency observed at low temperature. However, Fig. 4(d) shows that the first three eigenfrequencies are predicted to be affected equally by the change in membrane stress. So, this does not explain the lack of clear observation of the second resonant peak that was seen at room temperature.

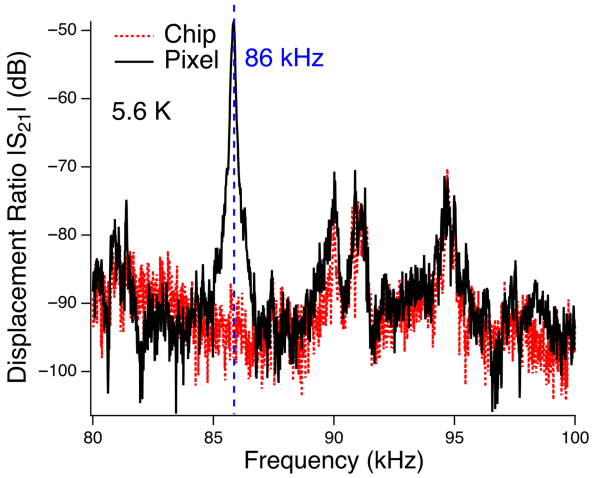


Fig. 7 $|S_{21}|$ as a function of excitation frequency measured by laser interferometry from reflection from the Si frame (red dashed) and the pixel absorber (black solid). As described in Sec. 2.2, $|S_{21}| \propto z_m/z_{pz}$ where z_m is the displacement magnitude in the z direction at the measurement point and z_{pz} is the displacement magnitude of the piezo actuators. Measured at 5.6 K.

4 Discussion

The results presented above demonstrate that, at room temperature, the first eigenfrequency in this microcalorimeter design is ∼89 kHz. The observed first eigenmode is in good agreement with the prediction from finite element modeling. The predicted first eigenfrequency is ∼17% lower than the measured value, which is remarkably good agreement given the simplifications of the design in the model, and the uncertainties in material properties. In particular, standard bulk properties were used for the Young's modulus, Poisson ratio, and density of the materials, but there may be significant deviations from those values in these thin fabricated layers. Also, the model is based on the fabrication masks used in the microfabrication of the devices, but in actual pixels, there may be deviations from this design by several microns in both dimensions in the $x - y$ plane and alignment of different layers. Figure 6 shows that, in general, the eigenfrequency is not highly sensitive to such small changes. However, one area where a dimension change of a few microns may be significant is in the size of the region where the Si is etched away to leave only the silicon nitride membrane. This sensitivity is shown in Fig. 6(b). The etch of the silicon is a time-dependent chemical process, and therefore, there can be some deviation from the specified design that could affect the eigenfrequencies. For example, the predicted first eigenfrequency is increased by ∼7% if the square back-etched region has a side length of 108 μm instead of the designed value of 110 μm.

At 6 K, the first eigenfrequency was measured at 86 kHz and therefore a few percent lower than the room temperature value. A significant effect of temperature was expected to be a decrease in the stress in the silicon nitride membrane due to the difference in the coefficient of thermal expansion between the Si and silicon nitride. The small decrease in the eigenfrequency observed is therefore broadly consistent with the prediction shown from modeling that the first eigenfrequency decreases with decreasing stress in the membrane. However, there are remaining questions about how the higher-order modes evolve with temperature and the impact of the temperature dependence of other material properties. The third eigenmode, observed at room temperature, was not observed at low temperature below 100 kHz contrary to the modeled prediction. It would be useful in the future to measure the eigenfrequencies up to higher frequencies at several temperatures between 300 and 6 K to determine the temperature dependence accurately and constrain the finite element model parameters. If possible, the use of the DHM to determine mode shapes at low temperatures would also be instructive.

The sensitivity of the first eigenfrequency to different pixel design parameters, shown in Fig. 6, provides input to future design decisions for X-IFU and other TES microcalorimeter instruments. In particular, this shows that if the absorber side length is increased, the eigenfrequency will decrease unless the absorber is better supported. The addition of more support stems

is undesirable because it would further increase the thermal conductance from the TES to the thermal bath of the silicon frame.[25,26] Therefore, the four corner support stems must be moved further apart and closer to the corners of the absorber. This in turn means the back-etched silicon nitride membrane region must be made larger. Figure 1 shows that in an array of TES pixels, the Si frame sections among silicon nitride membrane regions are where the Nb wires are placed. Therefore, if the silicon nitride membrane region is made too large, there will be insufficient space for all the wires needed for every pixel in the array. This is particularly true in very large arrays where a large number of wires must be placed on the frame. Hence, in large arrays, there must be a careful trade-off between the space required for wiring and the adequate support of the absorber to prevent unacceptably low eigenfrequencies.

The baseline pixel design for X-IFU has undergone several changes in the time since the fabrication of the prototype devices presented in this work. The square absorber side length has increased from 268 to 312 μm, the thickness of the Bi/Au bilayer of the absorber is now 5.5/1.0 μm, the TES width has reduced from 50 to 30 μm, and the four corner support stems for the absorber have moved further from the edge of the silicon nitride membrane region by 12 μm. These changes were driven by requirements unrelated to the vibrational response of the pixels[2,3] but are predicted to impact the first eigenfrequency of the design, as shown in Fig. 6. The larger side length of the absorber decreases the predicted first eigenfrequency, and the thicker Bi layer and thinner Au layer increase it slightly. The reduction of the width of the TES is predicted to have very little impact on the first eigenfrequency, but moving the corner stems away from the edge of the silicon nitride region lowers the first eigenfrequency significantly. In addition to these performance-driven changes, two other changes were made to the pixel design specifically to increase the first eigenfrequency. First, the position of the absorber was changed to be co-centered with the TES. This increases the symmetry of the system and raises the predicted first eigenfrequency by ∼8%. The second change was to increase the size of the back-etched silicon nitride membrane region from 110 to 160 μm. This allows the absorber support stems to be moved closer to the edge of the absorber, raising the first eigenfrequency, as shown in Fig. 6(b). With all these changes, finite element modeling predicts a first eigenfrequency in the new design of 49 kHz. Measurements of the eigenfrequencies of this new pixel design will be the subject of future work.

5 Conclusion

We have shown that the first eigenfrequency of TES microcalorimeter pixels designed for the X-IFU is 89 kHz at room temperature, decreasing to 86 kHz at 5.6 K. These results are in broad agreement with finite element modeling predictions of 74 kHz. The measured and predicted values are significantly larger than the X-IFU requirement of >25 kHz. This means that the first eigenfrequency is orders of magnitude larger than the expected bandwidth of known vibration sources, such as cryocoolers and the first eigenfrequencies of other low-temperature components in the system. We therefore expect negligible vibration coupling and dissipation in the pixels. Tests on X-IFU prototypes in the coming years will experimentally assess any significant dissipation effects at the pixels as well as other components of the instrument.

In addition, we identified some key differences between the modeled and measured vibration response, particularly in the higher-order modes and temperature dependence, which require further investigation. We also explored the predicted impact of design modifications on the first eigenfrequency, including recent changes to the X-IFU pixel design. Experimental validation of these modifications will be the focus of future work.

Disclosures

The authors declare there are no financial interests, commercial affiliations, or other potential conflicts of interest that have influenced the objectivity of this research or the writing of this paper.

Code and Data Availability

The data presented here are available upon request by contacting the authors at nwakeham@umbc.edu.

Acknowledgments

The material presented here is partly based upon work supported by the National Aeronautics and Space Administration (Grant No. 80GSFC24M0006). The large language model ChatGPT was consulted to improve the paper. A few isolated sentences were entered into ChatGPT along with a prompt asking to improve the grammar and clarity of the sentences.

References

1. D. Barret et al., "The Athena space X-ray observatory and the astrophysics of hot plasma," *Astronomische Nachrichten* **341**(2), 224–235 (2020).
2. D. Barret et al., "The Athena X-ray Integral Field Unit: a consolidated design for the system requirement review of the preliminary definition phase," *Exp. Astron.* **55**(2), 373–426 (2023).
3. P. Peille et al., "The X-ray Integral Field Unit at the end of the Athena reformulation phase," *Exp. Astron.* **59**(2), 1–36 (2025).
4. K. D. Irwin and G. C. Hilton, *Transition-Edge Sensors*, pp. 63–150, Springer Berlin Heidelberg, Berlin, Heidelberg (2005).
5. Y. Takei et al., "Vibration isolation system for cryocoolers of soft X-ray spectrometer on-board ASTRO-H (Hitomi)," *J. Astron. Telesc. Instrum. Syst.* **4**(1), 011216 (2018).
6. L. Gottardi et al., "A six-degree-of-freedom micro-vibration acoustic isolator for low-temperature radiation detectors based on superconducting transition-edge sensors," *Rev. Sci. Instrum.* **90**, 055107 (2019).
7. T. Hasebe et al., "Ground test results of the microvibration interference for the X-ray microcalorimeter onboard X-ray imaging and spectroscopy mission," *J. Astron. Telesc. Instrum. Syst.* **9**(1), 014003 (2023).
8. P. A. R. Ade et al., "Planck early results. II. The thermal performance of Planck," *Astron. Astrophys.* **536**, A2 (2011).
9. D. A. Girou et al., "Environmental testing of the Athena telescope mirror modules," *Proc. SPIE* **11822**, 1182209 (2021).
10. L. Ferrari Barusso et al., "First structural tests of the cryoac detector silicon chip of the Athena X-ray observatory," *Nucl. Instrum. Methods Phys. Res. Sect. A: Accel. Spectrom. Detect. Assoc. Equip.* **1047**, 167862 (2023).
11. E. Taralli et al., "The X-IFU focal plane assembly development model: microvibrations characterization," *Proc. SPIE* **13093**, 130930Z (2024).
12. K. Sakai et al., "Demonstration of a full-scale brassboard TES microcalorimeter array for the Athena X-IFU," *IEEE Trans. Appl. Supercond.* **33**(5), 1–5 (2023).
13. D. Davidovikj et al., "Visualizing the motion of graphene nanodrums," *Nano Lett.* **16**(4), 2768–2773 (2016).
14. E. Cuche, P. Marquet, and C. Depeursinge, "Simultaneous amplitude-contrast and quantitative phase-contrast microscopy by numerical reconstruction of Fresnel off-axis holograms," *Appl. Opt.* **38**, 6994–7001 (1999).
15. Y. Emery et al., "Digital Holographic Microscopy (DHM) for metrology and dynamic characterization of MEMS and MOEMS," *Proc. SPIE* **6186**, 61860N (2006).
16. W.-H. Chuang et al., "Mechanical property characterization of LPCVD silicon nitride thin films at cryogenic temperatures," *J. Microelectromech. Syst.* **13**(5), 870–879 (2004).
17. T. Kodas, "Handbook of chemical vapor deposition (CVD), principles, technology, and applications. By Hugh O. Pierson, Noyes, Park Ridge, NJ, 1992. 436 pp., hardback, $68, ISBN 0-8155-1300-3," *Adv. Mater.* **5**(5), 401–402 (1993).
18. J. G. Noel, "Review of the properties of gold material for MEMS membrane applications," *IET Circuits Devices Syst.* **10**(2), 156–161 (2016).
19. J. W. Arblaster, *Selected Values of the Crystallographic Properties of Elements*, ASM International (2018).
20. A Buch, *Pure Metals Properties: a Scientific and Technical Handbook*, ASM International, Materials Park, OH, USA (1999).
21. J. A. Dean and N. A. Lange, *Lange's Handbook of Chemistry*, Vol. 15 in Lange's Handbook of Chemistry, McGraw-Hill (1999).
22. W. Jiang et al., "Effect of hyperthermal annealing on LPCVD silicon nitride," *Mater. Sci. Semicond. Process.* **43**, 222–229 (2016).
23. S. Habermehl, "Coefficient of thermal expansion and biaxial Young's modulus in Si-rich silicon nitride thin films," *J. Vac. Sci. Technol. A* **36**, 021517 (2018).
24. A. K. Sinha, H. J. Levinstein, and T. E. Smith, "Thermal stresses and cracking resistance of dielectric films (SiN, Si_3N_4, and SiO_2) on Si substrates," *J. Appl. Phys.* **49**, 2423–2426 (1978).
25. M. de Wit et al., "High aspect ratio transition edge sensors for X-ray spectrometry," *J. Appl. Phys.* **128**, 224501 (2020).
26. N. A. Wakeham et al., "Refinement of transition-edge sensor dimensions for the X-ray integral field unit on Athena," *IEEE Trans. Appl. Supercond.* **33**(5), 1–6 (2023).

Biographies of the authors are not available.